




Electrostatic interactions between rough dielectric particlesMatthew Gorman , Xuan Ruan , and Rui Ni **Department of Mechanical Engineering, Johns Hopkins University, Baltimore, Maryland 21218, USA*

(Received 29 October 2023; accepted 23 January 2024; published 19 March 2024)

From colloid suspension to particle aggregation in protoplanetary formation, electrostatic attraction and repulsion between particles is a key mechanism behind the aggregation and clustering of particles. Although most studies have focused on canonical spherical particles, it remains unclear how nonspherical and rough dielectric particles interact and whether the complicated interplay between roughness and charge distribution affects their force couplings. Here a boundary-element method model was leveraged to study electrostatic interactions between charged dielectric particles with modular, axisymmetric surface features. Charge accumulation at convex surface asperities decreases the strength of electrostatic interactions between particles, and the sensitivity of the electrostatic force to the particle surface roughness and orientation is especially apparent at small particle separations. Surface interactions between the particle near-contact regions were isolated to determine the degree that near-contact interactions dictate the relationship between the net electrostatic force and the particle roughness and orientation. A correction factor ΔF is introduced to recover higher order dielectric effects from a low order analytical model. Finally, implications of surface charge asymmetries produced for different particle orientations and surface roughnesses on the long-standing problem of triboelectrification are discussed.

DOI: [10.1103/PhysRevE.109.034902](https://doi.org/10.1103/PhysRevE.109.034902)**I. INTRODUCTION**

Particle charges are present in many natural and industrial particle-laden flows, including dust in planet formations and on the lunar surface [1–4], sand in desert storms [5], ash in volcanic eruptions [6], powders in pharmaceutical processing plants [7], and contaminants in electrostatic precipitation filtration systems [8,9]. Often particles in these systems are charged triboelectrically through collisions with other particles or their surroundings [10,11]. They can also be charged by external ion fields or by UV radiation [12,13].

Electrostatic interactions between charged particles play important roles in each of these applications. In the early stages of planet formation, the electrostatic force enables millimeter-sized grains to overcome the bouncing barrier and form larger aggregates [14]. In desert storms, charged dust particles produce atmospheric electric fields that alter the concentration profiles of dust throughout the atmospheric boundary layer [5,15]. In industrial processing facilities, the buildup of static charge on particles leads to extreme explosion hazards [16]. In space exploration, electrostatic charges exacerbate the lunar dust problem, which remains a key impediment in the establishment of a long-term presence on the moon [17–19].

For particles composed of dielectric materials, induced polarizations effects can lead to drastic changes in the resulting electrostatic interactions. For example, for dielectric particles with similar polarity charges, increases in the dielectric constant can cause the force between the particles to

switch from repulsive to attractive provided that the difference in charge magnitude is sufficiently large [20,21]. Studies of the force between charged dielectric spheres indicate that induced polarizations increase the strength of the electrostatic interactions and minimizes the overall energy of the system, which can strongly influence particle assembly dynamics and clustering behaviors [22,23].

To the first order, polarizations can be approximated as dipole moments [24–26]. However, dipole approximations of the electrostatic force have been shown to be insufficient when the dielectric constant is large or the charge separations are small [27]. In such cases, higher order multipole interactions are required to accurately resolve electrostatic interactions, which adds significant complexity to an already complicated multibody problem. Moreover, existing models that consider induced multipoles are usually derived based on spherical geometries. In many applications, including those involving lunar dust [28], biomass [29], and volcanic ash particles [30], the nonsphericity of the particles plays a critical role. In these situations, it is difficult to directly extend spherical models to account for the nontrivial modulation due to irregular geometries. Therefore, different approaches are needed to resolve dielectric interactions between particles with complicated geometries.

Here we consider a simplified problem of the electrostatic interactions between a single pair of dielectric particles with modular surface roughness features. A boundary-element method (BEM) is employed to study the coupling between induced polarization effects and the surface roughness and orientation of the particles. The numerical method and the parameters of the pair-interaction study are first described. Then an analysis of the couplings between the geometric

*rui.ni@jhu.edu

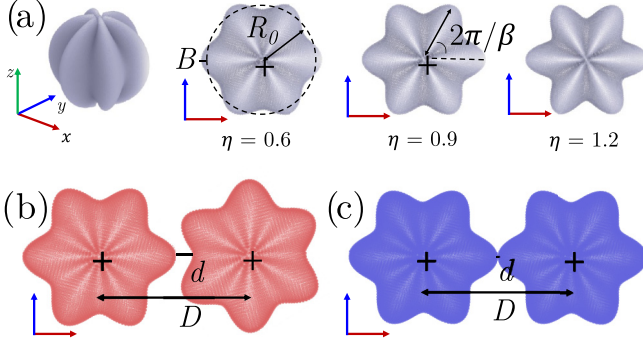


FIG. 1. (a) Geometry of the axisymmetric particles investigated in this study. From left to right, the roughness parameter $\eta = B\beta$ was varied by only increasing the amplitude B . The two critical orientations considered throughout this study are shown in panels (b) and (c). In the Mountain-Valley orientation colored red (b), a local “crest” on one particle’s surface aligns with a local “trough” on the neighboring particle’s surface. In the Mountain-Mountain orientation colored blue (c), the local surface crests of two adjacent particles are aligned.

characteristics of the particle surfaces and the resulting induced charge distribution and net electrostatic force is presented. Finally, implications of surface charge asymmetry that arise from geometric asymmetry in the near-contact region on the triboelectrification problem are discussed.

II. METHODS

A. Particle-pair interactions: Numerical method

A boundary-element method (BEM) that discretizes each particle geometry into surface patches was implemented to resolve particle surface charge distributions. [31]. Particle geometries were discretized into equally spaced patches using a force-based smoothing algorithm [32]. Results obtained with the BEM model were validated previously against two known analytical solutions: the electrostatic force between a point charge and a dielectric sphere and the force between two charged dielectric spheres. These and other details of the implemented BEM framework are provided in [27].

B. Particle-pair interactions: Key parameters

The particles considered in the study and the parameters used to characterize the pair interactions are shown in Fig. 1. The axes of both particles in the pair were always aligned with the z axis. The particle surface geometries are defined according to the equation $R = R_0[1 + B\sin(\beta\theta)]$, which produces a symmetric geometry about the azimuthal angle θ . The value of R_0 was set to unity for all particles considered in this study. The roughness of the particles is characterized by the amplitude B and the frequency β . By considering axisymmetric particles, the surface roughness of the particles can be varied without altering the particle aspect ratio or introducing any other large-scale geometric asymmetries. In this study, β was held constant at 6 and B was varied between 0 and 0.2.

A roughness parameter $\eta = B\beta$ was defined to measure the surface roughness of different particle geometries. Particles with different levels of surface roughness are shown in Fig. 1.

To investigate the influence of particle orientation on the electrostatic interactions, the left particle was fixed and the right particle was rotated about its z axis by the azimuthal angle θ . Two critical orientations were considered: the Mountain-Valley (MV) orientation, where $\theta = \pi/\beta$ and the crest of one particle aligns with the trough of the other, and the Mountain-Mountain (MM) orientation, where $\theta = 0$ and the crests of each particle are aligned. Blue and red symbols are used throughout this work to represent the MM and MV orientations, respectively. As shown in Fig. 1, the separation distance between the particles was measured as either D , the distance between the particle centers, or d , the shortest distance between the particle surfaces.

The value of the net particle charge, $\pm q$, was set to 7.07×10^{-14} C to match values of the average surface charge density measured in previous tribocharging experiments [6,23,33–35]. This value is also comparable to field measurements of the charge of ash particles in volcanic eruptions and sand particles in dust storms, and represents a conservative estimate of the charge on lunar dust from the *Apollo* missions [36–41]. The net particle charge was treated as a free surface charge and distributed uniformly over the particle surface. The particle free volume charge was zero for all cases. The vacuum dielectric constant κ_0 was set to 1, and the particle dielectric constant κ_p was set to 2.5 for both particles, which approximately matches the dielectric constant measured for lunar dust particles. [42].

The electrostatic force acting on a given particle is calculated by integrating the force acting on all the patch elements belonging to that particle. Throughout this work, F is normalized by the Coulomb force F_0 , where $F_0 = |\sigma_1||\sigma_2|R_0^2/\epsilon_0$ for particle pairs. Finally, the surface charge density is normalized by the scale $\sigma_0 = q/4\pi R_0^2$, which is the mean surface charge density for a spherical particle with the same total charge and radius R . The following sections provide details of the numerical method used to resolve the surface charge density.

C. Governing equation for the induced charge density

In the absence of a magnetic field, Maxwell’s equations can be simplified to

$$\nabla \cdot \mathbf{E} = -\rho/\epsilon_0 \quad (1)$$

and

$$\nabla \times \mathbf{E} = 0, \quad (2)$$

where \mathbf{E} is the electric field and ρ is the volumetric charge density. In dielectric materials, an induced polarization field \mathbf{P} partially cancels the applied electric field \mathbf{E} . The polarization field has an associated bound (or induced) volumetric charge density ρ_b that obeys the relationship [43]

$$\rho_b = -\nabla \cdot \mathbf{P}. \quad (3)$$

The total charge is the sum of the bound charge and the free charge ρ_f ,

$$\rho(\mathbf{r}) = \rho_f(\mathbf{r}) + \rho_b(\mathbf{r}), \quad (4)$$

where ρ_f is the net charge evenly distributed over the particle. For pure conductors, the free charge is the only charge present,

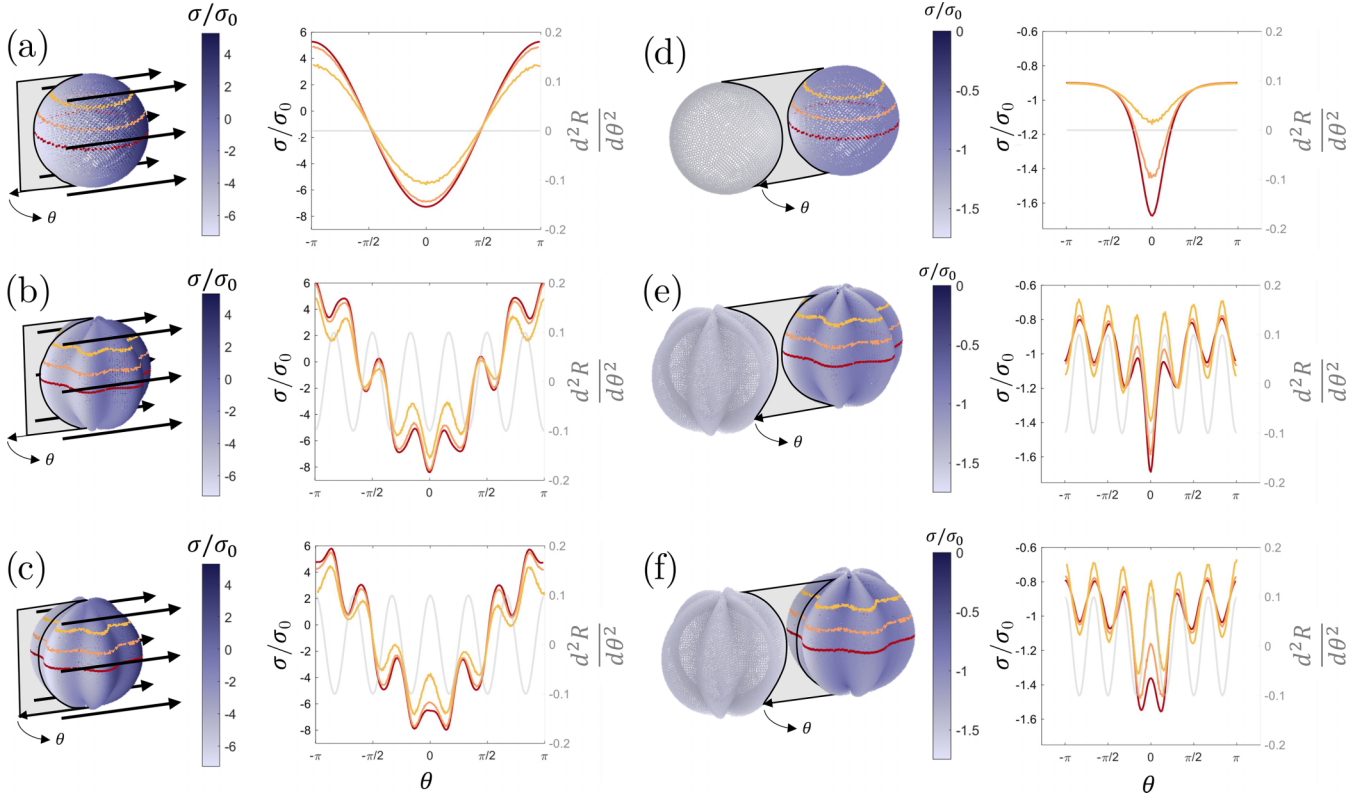


FIG. 2. Induced charge results visualized for select cases. (a–c) Surface charge distribution induced on an axisymmetric particle with a charge q in a constant external E field of magnitude $E = 10^{-5} q / (4\pi \epsilon_0 R_0^2)$ (indicated by the black arrows). (d–f) Surface charge distribution induced on an axisymmetric particle with a charge $-q$ in the external field produced by a nearby particle with a charge of $+q$, where the distance between the particle centers is $2.4R_0$. Each particle in the bottom panels (cases c and f) has been rotated 30° about its polar axis. The solid lines of the plots display the surface charge magnitude as a function of θ along three different horizontal contours distinguished by color, and the gray lines display the concavity as a function of the azimuthal angle θ along these same contours. For the single-particle cases shown in the left panels, $F_0 = qE_0$ and $E_0 = q / (4\pi \epsilon_0 R_0^2)$.

and the values of \mathbf{E} and \mathbf{P} inside the conductor are both zero [22].

For sharp dielectric interfaces, where changes in the dielectric constant κ are appreciable only at the material boundaries, the volumetric charge density reduces to the surface charge density σ_b [44]. A linear equation explicit in σ_b can then be formulated of the form

$$A\sigma_b = b, \quad (5)$$

where

$$A\sigma_b = \bar{\kappa}\sigma_b + \epsilon_0 \Delta\kappa \mathbf{E}_b \cdot \hat{\mathbf{n}} \quad (6)$$

and

$$b = (1 - \bar{\kappa})\sigma_f - \epsilon_0 \Delta\kappa \mathbf{E}_f \cdot \hat{\mathbf{n}}, \quad (7)$$

where $\bar{\kappa} = (\kappa_0 + \kappa_p)/2$, $\Delta\kappa = \kappa_0 - \kappa_p$, and κ_0 and κ_p are the dielectric constants of the surrounding vacuum and the particle, respectively. In Eq. (7), \mathbf{E}_b is the electric field component produced by the induced charge σ_b , and \mathbf{E}_f is the remaining component of the electric field from all other external sources such that $\mathbf{E} = \mathbf{E}_f + \mathbf{E}_b$.

In the present study, Eqs. (5), (6), and (7) are discretized in the BEM framework, and the surface charge on each patch is solved numerically.

The r.h.s. of Eq. (5) [Eq. (7)] contains the free charge terms, which are all known. In the l.h.s. of eq. 5 [Eq. (6)], an iterative scheme is employed to solve the coupled equation for \mathbf{E}_b [45]:

$$\mathbf{E}_b(\mathbf{r}) = \int_S \sigma_b(\mathbf{s})(\mathbf{r} - \mathbf{s}) / (4\pi \epsilon_0 |\mathbf{r} - \mathbf{s}|^3) ds, \quad (8)$$

Once the total surface charge σ has been resolved on each particle, the electrostatic force on each patch can be computed, and the net electrostatic force acting on a particle is calculated by summing the force acting on all the patch elements belonging to that particle. The remaining discussion focuses on the impact of particle roughness and orientation on the net force between particle pairs.

III. RESULTS

Induced surface charge results for selected cases are shown in Fig. 2 and quantified in Table I. Figures 2(a), 2(b), and 2(c) show induced charge results for individual particles subjected to a constant uniform external E field. The arrows indicate the direction of the E field. Despite changes in particle geometry, orientation, and the induced surface charge distribution, the net electrostatic force (provided in Table I) remains constant between these cases. Because the net particle charge is a conserved quantity and is fixed between all cases, the effects

TABLE I. Results from selected cases.

| Case | η | Orientation | Charge | E/E_0 | D/R_0 | F/F_0 | F_{CA}/F | $ \sigma_{\max} /\sigma_0$ (L/R) | N_{CA}/N_p (L/R) |
|------|--------|-------------|----------|-----------|---------|------------------------|------------|----------------------------------|---------------------|
| a | 0 | NA | $-q$ | 10^{-5} | NA | 1.437×10^{-4} | NA | 7.276 | NA |
| b | 0.6 | MM | $-q$ | 10^{-5} | NA | 1.437×10^{-4} | NA | 8.396 | NA |
| c | 0.6 | MV | $-q$ | 10^{-5} | NA | 1.437×10^{-4} | NA | 7.970 | NA |
| d | 0 | NA | $+q - q$ | NA | 2.4 | -1.15546 | 0.312112 | (1.55697/1.55674) | (0.2498/0.250) |
| e | 0.6 | MM | $+q - q$ | NA | 2.4 | -1.1005 | 0.27464 | (1.81614/1.81773) | (0.228631/0.227013) |
| f | 0.6 | MV | $+q - q$ | NA | 2.4 | -1.07077 | 0.258652 | (1.69797/1.49983) | (0.228631/0.229107) |

of all induced charges cancel for a single particle in a uniform electric field. Consequently, the electrostatic force for these cases is only a function of the net particle charge, not the charge distribution, the geometry, or the orientation of the particle, which is confirmed in the present results.

The single-particle cases also demonstrate an intriguing coupling between the surface concavity and the surface charge distribution. At the global particle scale, each particle exhibits charge segregation across the entire particle geometry that is aligned with the direction of the external field: positive values of σ concentrate farther down-field, and negative values of σ concentrate farther up-field. This observation qualitatively matches the results of the induced charge obtained for electrostatic interactions between dielectric spheres [27,45]. However, at the roughness element scale, the rough particles exhibit oscillations in σ that appear to be in phase with oscillations in the surface concavity, $d^2R/d\theta^2$. This result, shown in the contour plots in Fig. 2, provides qualitative evidence for the correlation between local surface charge and surface curvature and concavity, as proposed in [27].

The surface charges induced between charged particle pairs, shown in Figs. 2(d), 2(e), and 2(f), have several key differences compared to the single particle cases. For the spherical case shown in Fig. 2(d), the gradient of charge shows a sharp decrease in the near-contact region around $\theta = 0$, where surface separations are minimized. Similar observations can be made for the rough particles shown in Figs. 2(e) and 2(f): at the global particle scale, the surface charge shows a sharp decline at the near-contact region instead of a gradual change. However, like the single-particle cases, higher frequency oscillations in σ are still present across the entire particle surface and appear to be in phase with the surface concavity.

A. Electrostatic force

The electrostatic force was obtained by integrating the force acting on all patches belonging to that particle according to the expression [45,46]

$$\mathbf{F} = \int_S \kappa_0(\sigma_f + \sigma_b)\mathbf{E} dS. \quad (9)$$

Figure 3(a) shows the electrostatic force produced between pairs of dielectric particles with the same magnitude charge but opposite polarity, i.e., $(+q, -q)$. The particle surface roughness, particle orientation, and the separation between the particles were varied between cases. The cases where induced charge effects are strongest are highlighted in the inset of Fig. 3(a).

Three conclusions can be drawn from Fig. 3(a). The first conclusion is that the force magnitude is significantly larger between the spherical pairs than between any of the rough particle pairs. Second, the electrostatic force is sensitive to the particle orientation: at a fixed center-center separation,

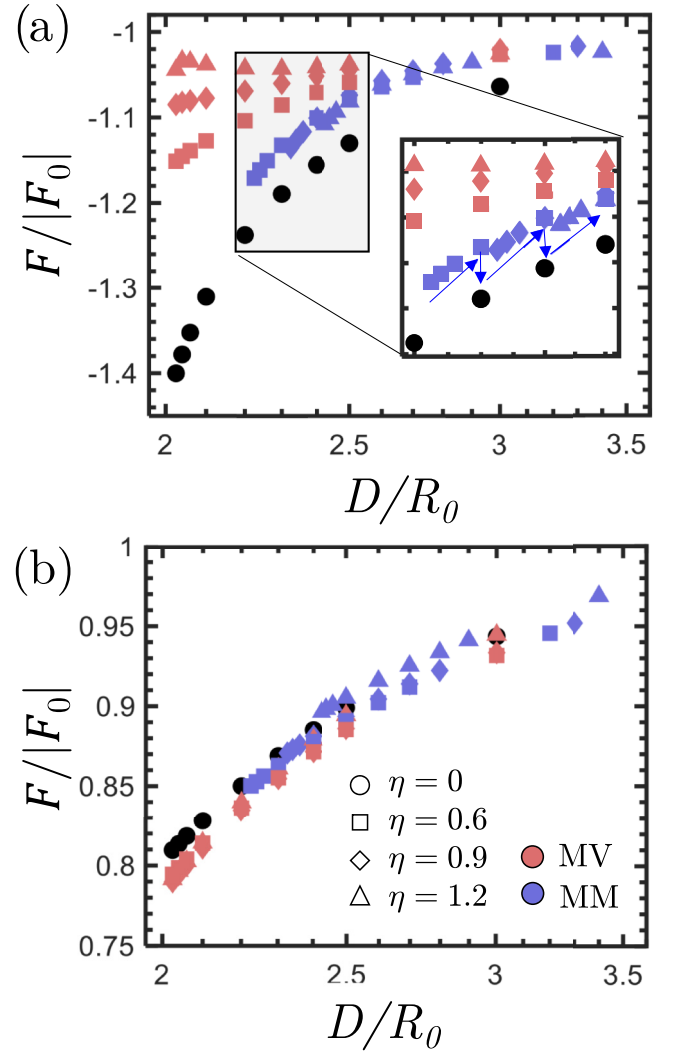


FIG. 3. Normalized force $F/|F_0|$ between (a) oppositely charged particles $(+q, -q)$ and (b) similarly charged particles $(+q, +q)$ as a function of the separation between particles. Red markers indicate the MV orientation, and blue markers indicate the MM orientation. The marker type distinguishes different values of the surface roughness: squares correspond to $\eta = 0.6$, diamonds to $\eta = 0.9$, and triangles to $\eta = 1.2$.

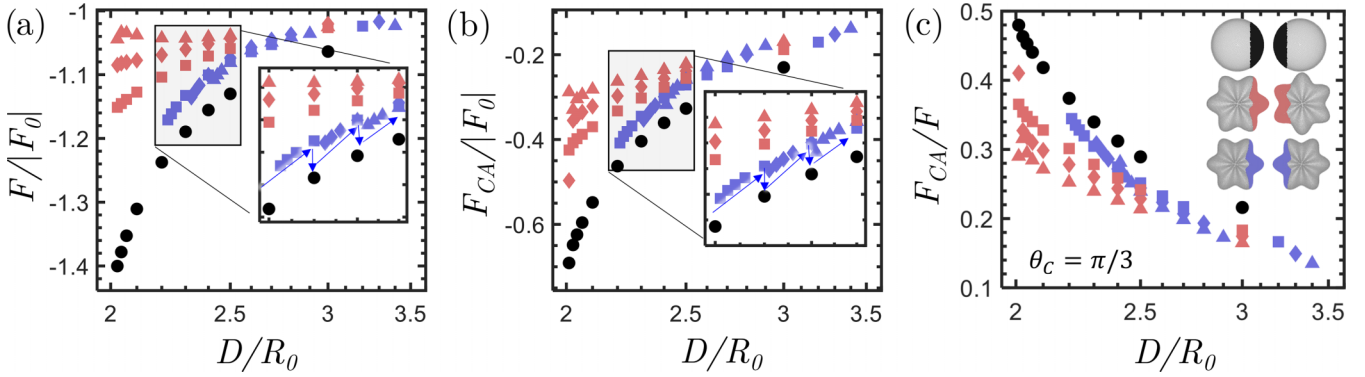


FIG. 4. Comparison between the net force between particles when all particle surface patch interactions are included in the force calculation (a) and when only the near-contact region surface patches are included (b). The electrostatic force between the point charge approximations of the particle near-contact regions relative to the full electrostatic force. Marker colors and symbols have the same significance as in Fig. 3. In the particle pairs shown in the inset of panel (c), the particle near-contact regions are colored according to the orientation of the particle pair. The near-contact region is defined as all particle patches located within an angle θ_c of the axis connecting the centers of the two particles.

particles in the MM configuration experience a stronger force than particles in the MV orientation. The final conclusion is that F and the roughness parameter η are positively correlated for the MM orientation but negatively correlated for the MV orientation.

We now show the significant influence of the near-contact region on the overall interaction between the particle pair. The force between surface patch elements is given by the expression

$$F_{CA} \sim \kappa |q_1| |q_2| / d_{12}^2, \quad (10)$$

where $\kappa = 1/(4\pi\epsilon_0)$, q_i is the net charge of surface patch i , and d_{ij} is the separation distance between the surface patches. The $1/d^2$ dependence of this relationship, as well as the observed charge accumulation near $\theta = 0$ shown in Fig. 2, indicate that the surface interactions between the near-contact region patches are dominant relative to other patch interactions. For the present results, the near-contact region is defined as all surface patches on the contact side of the particle that reside within an angle θ_c of the axis connecting the centers of the two particles where θ_c is equal to $\pi/3$. For the example cases depicted in Fig. 2, the number of near-contact patches (N_{CA}) for the left and right particle of the pair is shown in the final column of Table I.

The results shown in Fig. 4 illustrate that surface interactions between the near-contact regions are dominant relative to the interactions between other patches, especially at small separations. Figure 4(a) shows force results when all surface patch interactions are considered, and Fig. 4(b) shows results when only the near-contact region patch interactions are considered. The observed relationship between F_{CA} and the surface roughness η , separation distance D , and orientation of the particle pairs are nearly identical to the relationships observed for F . Figure 4(c) shows the ratio F_{CA} to F , and Table I quantifies this ratio for the selected cases.

Figure 3(b) shows the electrostatic force between similarly charged ($+q + q$) particles. In contrast to the oppositely charged ($+q, -q$) cases, where polarization effects enhance electrostatic interactions, a reduction in the repulsive force is apparent for all similar charge cases. Unlike the oppositely charged pairs, the spherical case does not exhibit significantly

different results relative to the rough cases. Furthermore, no monotonic relationship is evident between the magnitude of the repulsive force and the surface roughness parameter η , and differences between the MM and MV orientations are negligible.

Unlike the ($+q, -q$) cases, interactions between the ($+q, +q$) particle pairs are not dominated by the near-contact region interactions. While induced polarizations between oppositely charged particles accumulates charges at the near-contact region and produce an attractive force enhancement, induced polarizations between similarly charged particles push surface charges away from the near-contact region and reduce the strength of the repulsive force. This explains why the curves in Fig. 3(b) collapse for all cases.

B. Force correction ΔF

The results shown thus far demonstrate that induced polarizations strongly influence the electrostatic interactions between dielectric particles. However, solving the effective multibody problem to resolve the induced charge in the BEM model is costly and often impractical for large-scale simulations. To provide a more practical means of recovering higher order induced charges, a force correction factor ΔF was defined as the difference between the force predicted by an analytical point-charge dipole (PCD) model and the force computed using the full BEM model. The PCD model recovers low-order polarization effects by modeling particles as a superposition of a point charge (monopole) and a dipole [47]. The electric field in the PCD model is given by

$$\mathbf{E}(\mathbf{x}_i) = \sum_{j \neq i} \left[\frac{q_j \mathbf{r}_{ij}}{4\pi\epsilon_0 r_{ij}^3} - \nabla \left(\frac{\mathbf{p}_j \cdot \mathbf{r}_{ij}}{4\pi\epsilon_0 r_{ij}^3} \right) \right], \quad (11)$$

where q_i is the charge of a particle located at x_i and r_{ij} is the distance between particles i and j . The induced dipole \mathbf{p}_i , which is assumed to be linearly dependent on the local field strength, is given by

$$\mathbf{p}_i = 4\pi\epsilon_0 r_p^3 \frac{\kappa_p - \kappa_0}{\kappa_p + 2\kappa_0} \mathbf{E}(\mathbf{x}_i). \quad (12)$$

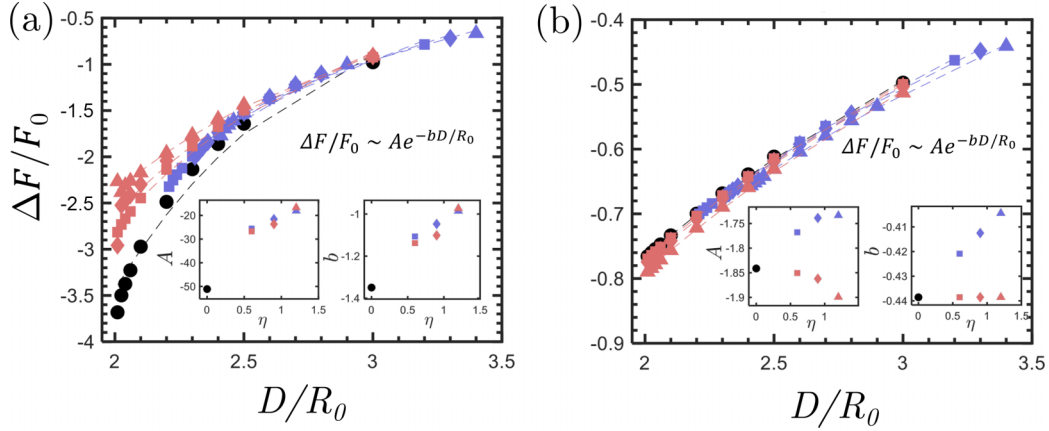


FIG. 5. Force correction factor ΔF vs separation distance for opposite polarity particles (a) and same polarity particles (b), where the charge magnitude on each particle is constant. The significance of the colors and symbols is consistent with Fig. 3.

After an iterative method is used to calculate the electric field, the force predicted by the PCD model is given as

$$\mathbf{F}_{E,i} = q_i \mathbf{E}(\mathbf{x}_i) + \mathbf{p}_i \cdot \nabla \mathbf{E}(\mathbf{x}_i). \quad (13)$$

Further details of the PCD model are provided in [27,48].

The PCD analytical model is much less computationally expensive than the full BEM model, but recovers only low order induced charge effects [27]. The induced dipole portion of the PCD model is valid only for spherical particles. Therefore, this model only captures first-order polarization effects, and is incapable of resolving higher order effects that arise from variations in the particle surface geometry. The force correction factor ΔF provides a means to recover the full BEM model force results between particle pairs at the same low computational cost as the PCD model. The expression for ΔF is given by

$$\Delta F = |F| - |F_{\text{PCD}}|, \quad (14)$$

where $|F|$ is the magnitude of the force computed from the BEM model and $|F_{\text{PCD}}|$ is the magnitude of the force predicted by the PCD model [Eq. (13)].

Values of ΔF for different cases are shown in Fig. 5. The left panels shows the force correction factor for particles with opposite polarity net charges, and the right panels shows the force correction factor for particles with identical polarity net charges.

As the separation distance between particles increases, the $\Delta F/F_0$ vs D data collapse for all cases. This indicates that the polarization effects are insensitive to a particle's roughness or orientation when the particle separation distance is sufficiently large. The present results suggest that separation distances greater than approximately $20B$ are necessary for the roughness effects to become negligible.

At closer separations, the magnitude of ΔF decreases as η increases, indicating that higher order polarization effects are mitigated for rough particle surfaces. Local minima and maxima in the surface concavity of rough particles serve as preferred locations for charges to concentrate, and prevent larger scale and stronger polarizations. This is supported by the results in Fig. 2, where smaller values of σ are produced for rough particles relative to the spherical particles.

As D approaches infinity, the value of ΔF approaches zero for both the PCD model and the BEM model. Equations of the form $\Delta F/F_0 = Ae^{bD}$ were fit to the data to recover the general shape of the $\Delta F/F_0$ data observed in Fig. 5 and the horizontal asymptote at infinite separation distances. The values of the fitting parameters A and b are shown in the inset panels of Fig. 5. The parameter A controls the magnitude of ΔF , and the parameter b captures the gradient of the increase in $|F|$ at small separations. For the opposite charge cases, both fitting parameters show linear trends with the roughness parameter η for the opposite charge cases. This indicates that surface roughness reduces both the magnitude of the attractive force and the gradient of the force increase at small particle separations. However, for similar charge cases, A becomes less sensitive to η compared to the opposite charge cases: the magnitude of b is approximately half the value for the opposite charge cases. These findings are consistent with the results in Fig. 3, which show that the difference in F for different surface roughnesses particles is minimal for the similar charge case, and that the increase in F at small separations is much less pronounced relative to the opposite charge cases. Our numerical data sets provide a simple way to capture the high-order correction, ΔF , between particles. Extensions of these studies may provide a method to predict ΔF between particle geometries characterized by β , η , or other generic orientation and surface roughness parameters.

C. Local surface charge distribution

An analysis of the local surface charge distribution across the particle surfaces provides further insight into the coupling between electrostatic interactions and particle orientation and surface roughness. The local charge distributions were extracted across the section of the equator contours, which are visualized as red bands in Fig. 2. These distributions are shown in Fig. 2.

The MV and MM orientations are shown in Figs. 6(a) and 6(b), respectively. The gray cut planes show the location of the equator contours, and the charge distribution along the equator contours are shown in the right plots. In both the visualized particles and the right contour plots, the gray colorbar indicates the value of $|\sigma|$. The surface charges at d_{min} for the left

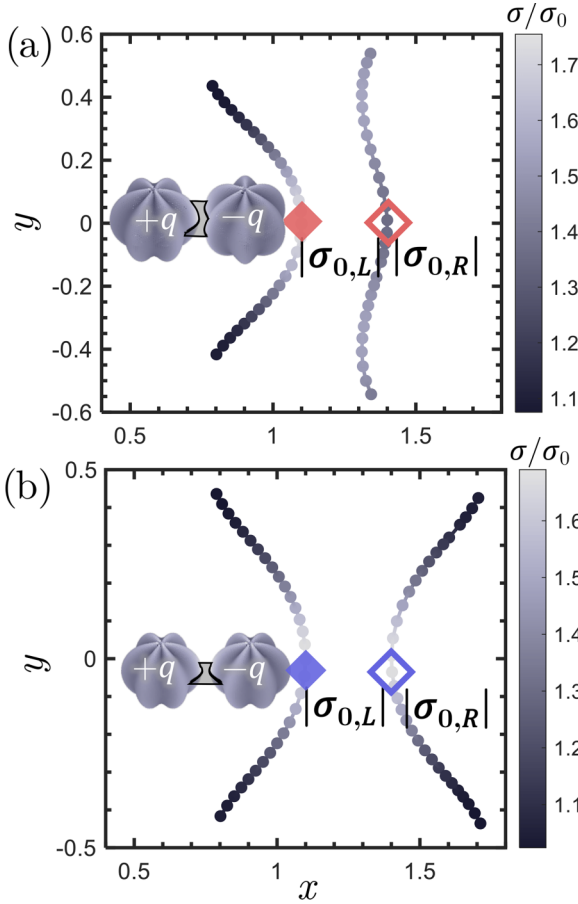


FIG. 6. Charge distribution over the equator contours of oppositely charged particles in (a) the MV orientation and (b) the MM orientation. The gray cut planes in the left panels illustrate the location of the extracted equator contours. Closed symbols represent the left particle in the pair, and open symbols represent the right particle in the pair. The symbol shapes and colors are consistent with those in Fig. 3.

and right particles ($\sigma_{0,L}$ and $\sigma_{0,R}$, respectively) are plotted in Fig. 7. Open symbols correspond the right particle of the pair, and closed symbols correspond the left particle. The color and shape of the symbols correspond with the legend in Fig. 3.

While the MM configuration always produces symmetric charge distributions, asymmetry in charge distribution appears for the MV configuration as shown in Fig. 6(a). For the left particle, the value of σ_{\max} is located at $y \sim 0$, which is the approximate location of d_{\min} . On the other hand, the value of σ_{\max} for the right particle is located at $y \sim \pm 0.4R_0$, which corresponds to the approximate locations of that particle's nearest surface crests. These findings support the hypothesis that the tendency for charges to accumulate at local crests competes with the tendency for charges to accumulate at the location of d_{\min} . For the MM cases, these two effects are not in competition, σ_{\max} always coincides with the location of d_{\min} at $y \sim 0$.

For the opposite charge polarity cases shown in Fig. 7(a), the MM configuration produces identical values of $|\sigma_{0,L}|$ and $|\sigma_{0,R}|$ due to the geometric symmetry of this orientation. However, for the MV cases, the value of $\sigma_{0,L}$ is consistently larger

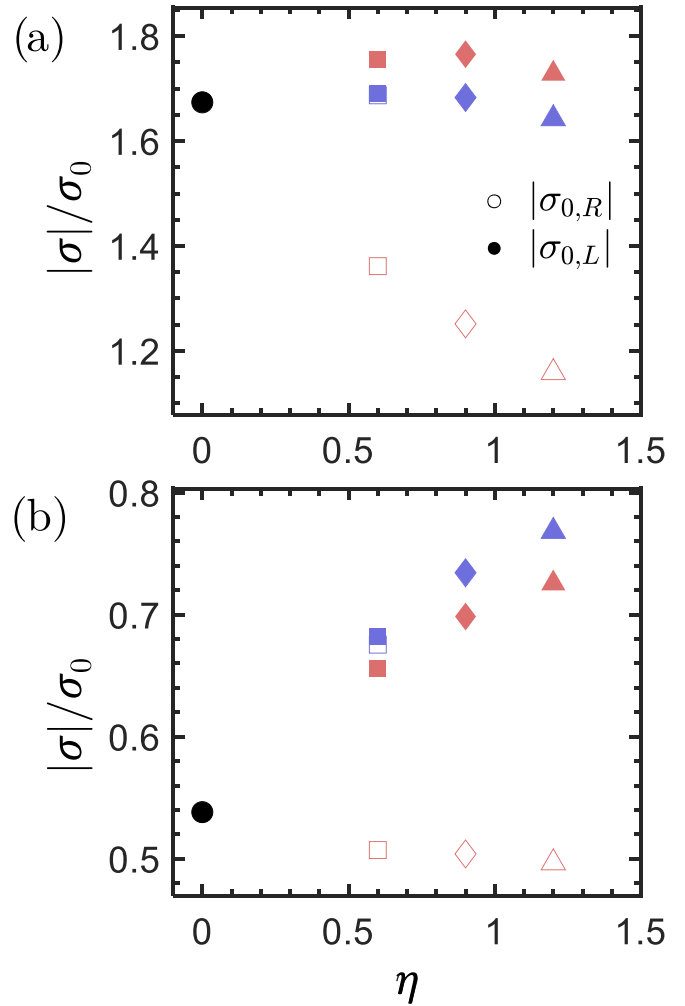


FIG. 7. The magnitude of the surface charge density $|\sigma|$ at the points corresponding to $y = 0$ for (a) opposite charge polarity particles and (b) similar charge polarity particles. The symbol shapes and colors are consistent with those in Fig. 3. Closed symbols represent the left particle in the pair, and open symbols represent the right particle in the pair.

than $\sigma_{0,R}$ due to the asymmetry in charge distribution. The difference between $\sigma_{0,L}$ and $\sigma_{0,R}$ increases as η increases. This indicates that the “sharpness” of the surface roughness asperity determines the intensity of charge concentration at a local surface crest.

Similar trends are observed for the similar charge polarity cases shown in Fig. 7(b): the MM configuration produces identical values of σ_0 for the left and right particles, and the difference $|\sigma_{0,R} - \sigma_{0,L}|$ for the MV configuration increases as η increases.

D. Implications for triboelectrification models

As shown in the surface charge distribution results in Figs. 6 and 7, changes in particle orientation can introduce asymmetries in the charge distributions between the near-contact regions of the particle pair. These asymmetries have implications for the complex and long-standing problem of triboelectric charging, as the surface charge difference

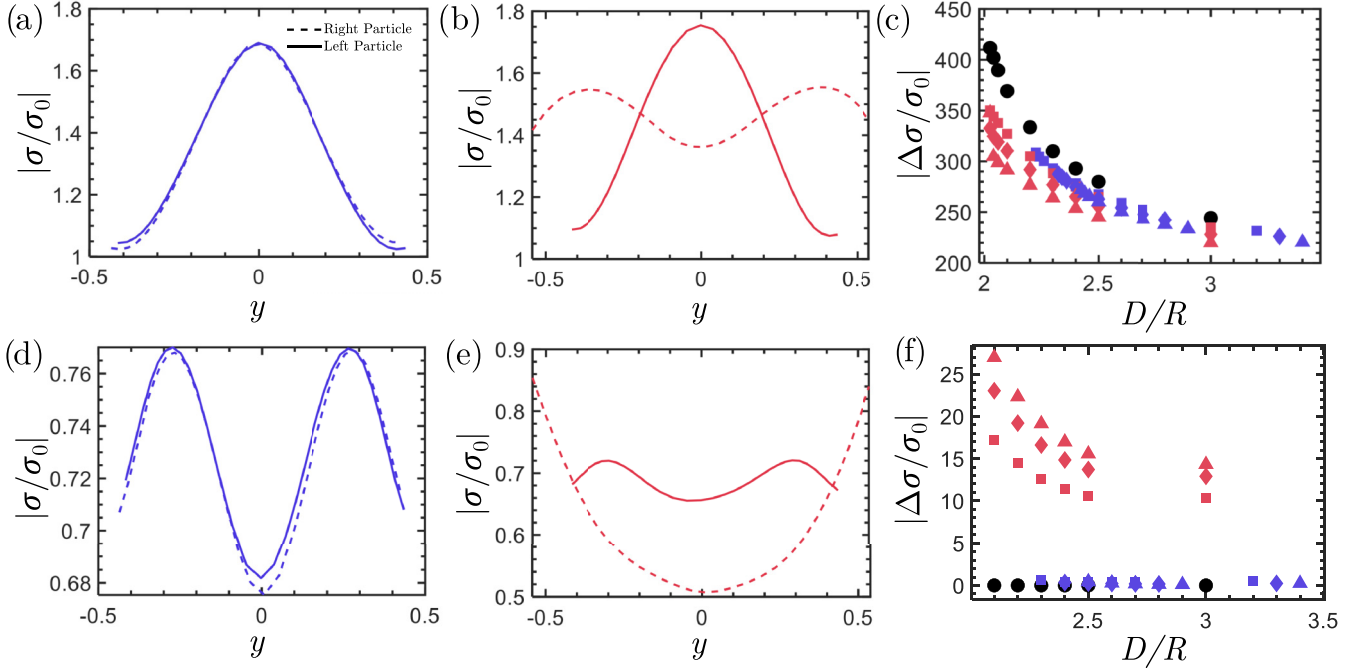


FIG. 8. Induced charge results across the equator contours. Opposite charge polarity cases ($+q, -q$) are shown in the top row, plots (a), (b), and (c), and similar charge polarity cases ($+q, +q$) are shown in the bottom row, plots (d), (e), and (f). The magnitude of the charge density along the equator contours as a function of y are shown for particle pairs with $\eta = 0.6$, $D = 2.3$ are shown in plots (a), (b), (d), and (e), where the orientation of the particles is indicated in the legend. Values of the net charge difference between the equator contours, $\Delta\sigma$, are shown in plots (c) and (f) for the MM/MV orientations and for different values of η and D . The symbol shapes and colors are consistent with those in Fig. 3.

between individual grains of colliding surfaces is one of the factors that governs the charge transfer during collisions [49].

The surface charge distribution across the equator contours for particle pairs with $\eta = 0.6$ and $D = 2.3$ are shown in Figs. 8(a), 8(b), 8(d), and 8(e). Results in the top row of Fig. 8 are for particle pairs with opposite polarities ($+q, -q$), and results in the bottom row are for particles with similar charge polarities ($+q, +q$).

The surface charge $|\sigma|(y)$ is almost perfectly symmetric for the MM orientation cases, as shown by the collapse of the $|\sigma|(y)$ curves in Figs. 8(a) and 8(d), whereas the charge distributions do not collapse for the MV orientation cases in Figs. 8(b) and 8(e). For all cases, peak values of $|\sigma|$ correspond to the locations of each particle's surface crests.

These results indicate total charge difference between neighboring contours (and, by extension, between the near-contact regions) is highly sensitive to the orientation of the particles. To measure the net charge difference between the contours, the parameter $\Delta\sigma$ is defined as

$$\Delta\sigma = \int_{y_c} |\sigma_{c,R}(y) - \sigma_{c,L}(y)| dy, \quad (15)$$

where y_c is the shared y range of the equator contours within each particle's respective near-contact region and $\sigma_{c,L}$ and $\sigma_{c,R}$ are the charge distributions across the equator contours of the left and right particles, respectively. Figure 8 shows $\Delta\sigma$ for particles with opposite polarities [Fig. 8(c)] and same polarities [Fig. 8(f)].

For the opposite polarity cases in Fig. 8(c), the value of $\Delta\sigma$ is large for all cases. Although the asymmetries in $|\sigma|$ shown in Fig. 8(b) are absent in Fig. 8(a), the overall charge difference is still large for all cases due to the opposite polarities, and relatively little variation in $\Delta\sigma$ is evident as the orientation or roughness of the particle pairs is varied. However, for the similar polarity cases in Fig. 8(f), the asymmetries that result from orientation differences are much more significant. The MV configuration increases $\Delta\sigma$ that differ by nearly an order of magnitude relative to the MM orientation cases, in which the contour charge distributions are nearly identical and $\Delta\sigma \sim 0$. These results illustrate the critical role that particle orientation plays in collisional charge transfer between rough particles: asymmetric charge distributions can lead to large increases in the net charge difference between the contact surfaces of colliding particles.

In many models of triboelectric charging, including the condenser or capacitor model [50–53], the dipole induction model [54,55] the Q-patch or mosaic charge acceptor or donor model [56–59], and the charge relaxation model [60,61], the initial difference in surface charge at the surface contact point determines the charge transfer between the surfaces. However, discrete-element models that include triboelectric charging often model particles as perfect spheres to simplify collision models [62]. The present results indicate that this simplification eliminates orientation-dependent surface charge asymmetries, and could lead to drastic underpredictions in the charge transfer between the particles.

IV. CONCLUSION

The dynamics of particle-laden flows are affected by the geometric features and the nonuniform surface charge distribution over dielectric particles. However, calculations of the surface charge distribution, which is known to exhibit complex and sometimes competing dependencies on both the local surface roughness and the surrounding E field, presents a significant obstacle to resolving these dynamics.

The coupling between surface roughness and charge distribution over dielectric particles was studied through the interaction of a pair of charged particles with modular surface roughness features. A BEM framework was used to numerically calculate the dielectric interactions between the charged particles. Because the BEM framework is robust for any scale or geometry, the results of this study are generic and can be applied to real particles, which typically have asymmetric shapes and finer-scale roughness features.

The electrostatic force between oppositely charged particles exhibited complex coupling to both the roughness and orientation of the particles. However, the repulsive

electrostatic interactions between similarly charged particles showed minimal dependency on surface roughness or orientation. A parameter ΔF was introduced to recover the BEM results for higher order electrostatic force interactions between particle pairs at a reduced computational cost.

Finally, implications of asymmetric surface charge distributions produced by variations in particle surface roughness and orientation on triboelectrification were discussed. Here asymmetries were shown to augment surface charge differences between particle surfaces by nearly an order of magnitude, potentially leading to similarly drastic increases in collisional charge transfers. This highlights the importance of accounting for surface asperities in triboelectrification models and may contribute to the large particle charges present in many high-energy particle-laden flow applications.

ACKNOWLEDGMENT

We wish to acknowledge support from NASA ESI Grant No. 80NSSC21K0222.

-
- [1] G. Wurm and J. Teiser, Understanding planet formation using microgravity experiments, *Nat. Rev. Phys.* **3**, 405 (2021).
 - [2] X. Wang, J. Schwan, H.-W. Hsu, E. Grün, and M. Horányi, Dust charging and transport on airless planetary bodies, *Geophys. Res. Lett.* **43**, 6103 (2016).
 - [3] G. Arrhenius, S. Asunmaa, and R. Fitzgerald, Electrostatic properties of lunar regolith, in *Abstracts of the Lunar and Planetary Science Conference* (Lunar and Planetary Institute, La Jolla, CA, 1972), Vol. 3, p. 30.
 - [4] G. Heiken, D. Vaniman, and B. M. French, *Lunar Sourcebook: A User's Guide to the Moon* (Cambridge University Press, New York, 1991).
 - [5] F. Esposito, R. Molinaro, C. I. Popa, C. Molfese, F. Cozzolino, L. Marty, K. Taj-Eddine, G. Di Achille, G. Franzese, S. Silvestro, and G. G. Ori, The role of the atmospheric electric field in the dust-lifting process, *Geophys. Res. Lett.* **43**, 5501 (2016).
 - [6] J. M. Harper and J. Dufek, The effects of dynamics on the triboelectrification of volcanic ash, *J. Geophys. Res.: Atmos.* **121**, 8209 (2016).
 - [7] J. Wong, P. C. L. Kwok, and H.-K. Chan, Electrostatics in pharmaceutical solids, *Chem. Eng. Sci.* **125**, 225 (2015).
 - [8] E. J. Shaughnessy, J. H. Davidson, and J. C. Hay, The fluid mechanics of electrostatic precipitators, *Aerosol Sci. Technol.* **4**, 471 (1985).
 - [9] K. Adamiak, Numerical models in simulating wire-plate electrostatic precipitators: A review, *J. Electrostat.* **71**, 673 (2013).
 - [10] S. Matsusaka, H. Maruyama, T. Matsuyama, and M. Ghadiri, Triboelectric charging of powders: A review, *Chem. Eng. Sci.* **65**, 5781 (2010).
 - [11] N. Mujica and S. Waitukaitis, Accurate determination of the shapes of granular charge distributions, *Phys. Rev. E* **107**, 034901 (2023).
 - [12] Z. Long and Q. Yao, Evaluation of various particle charging models for simulating particle dynamics in electrostatic precipitators, *J. Aerosol Sci.* **41**, 702 (2010).
 - [13] S. I. Popel and L. M. Zelenyi, Future lunar missions and investigation of dusty plasma processes on the moon, *J. Plasma Phys.* **79**, 405 (2013).
 - [14] J. Teiser, M. Kruss, F. Jungmann, and G. Wurm, A smoking gun for planetesimal formation: Charge-driven growth into a new size range, *Astrophys. J. Lett.* **908**, L22 (2021).
 - [15] V. Daskalopoulou, S. A. Mallios, Z. Ulanowski, G. Hloupis, A. Gialitaki, I. Tsikoudi, K. Tassis, and V. Amiridis, The electrical activity of Saharan dust as perceived from surface electric field observations, *Atmos. Chem. Phys.* **21**, 927 (2021).
 - [16] A. Ohsawa, Statistical analysis of fires and explosions attributed to static electricity over the last 50 years in Japanese industry, *J. Phys. Conf. Series* **301**, 012033 (2011).
 - [17] J. R. Gaier, The effects of lunar dust on EVA systems during the Apollo missions, Tech. Rep. NASA/TM-2005-213610, NASA Glenn Research Center, Cleveland, Ohio (2005).
 - [18] R. Caston, K. Luc, D. Hendrix, J. A. Hurowitz, and B. Demple, Assessing toxicity and nuclear and mitochondrial DNA damage caused by exposure of mammalian cells to lunar regolith simulants, *GeoHealth* **2**, 139 (2018).
 - [19] D. Budzyń, E. Tuohy, N. Garrivier, T. Schild, A. Cowley, R. Cruise, M. Adachi, H. Zare-Behtash, and A. Cammarano, Lunar dust: Its impact on hardware and mitigation technologies, in *Proceedings of the 46th Aerospace Mechanisms Symposium* (NASA Johnson Space Center, 2022), pp. 287–300.
 - [20] E. Bichoutskaia, A. L. Boatwright, A. Khachatourian, and A. J. Stace, Electrostatic analysis of the interactions between charged particles of dielectric materials, *J. Chem. Phys.* **133**, 024105 (2010).
 - [21] A. F. V. Matias, T. Shinbrot, and N. A. M. Araújo, Mechanical equilibrium of aggregates of dielectric spheres, *Phys. Rev. E* **98**, 062903 (2018).
 - [22] K. Barros and E. Luijten, Dielectric effects in the self-assembly of binary colloidal aggregates, *Phys. Rev. Lett.* **113**, 017801 (2014).
 - [23] V. Lee, S. R. Waitukaitis, M. Z. Miskin, and H. M. Jaeger, Direct observation of particle interactions and clustering

- in charged granular streams, *Nat. Phys.* **11**, 733 (2015).
- [24] J. Kolehmainen, A. Ozel, Y. Gu, T. Shinbrot, and S. Sundaresan, Effects of polarization on particle-laden flows, *Phys. Rev. Lett.* **121**, 124503 (2018).
- [25] J. Abrahamson and J. Marshall, Permanent electric dipoles on gas-suspended particles and the production of filamentary aggregates, *J. Electrostat.* **55**, 43 (2002).
- [26] X. Qian, X. Ruan, and S. Li, Effect of interparticle dipolar interaction on pore clogging during microfiltration, *Phys. Rev. E* **105**, 015102 (2022).
- [27] X. Ruan, M. T. Gorman, S. Li, and R. Ni, Surface-resolved dynamic simulation of charged non-spherical particles, *J. Comput. Phys.* **466**, 111381 (2022).
- [28] W. Carrier III, J. K. Mitchell, and A. Mahmood, The nature of lunar soil, *J. Soil Mech. Found. Division* **99**, 813 (1973).
- [29] H. Cui and J. R. Grace, Fluidization of biomass particles: A review of experimental multiphase flow aspects, *Chem. Eng. Sci.* **62**, 45 (2007).
- [30] L. Wilson and T. C. Huang, The influence of shape on the atmospheric settling velocity of volcanic ash particles, *Earth Planet. Sci. Lett.* **44**, 311 (1979).
- [31] D. Boda, D. Gillespie, W. Nonner, D. Henderson, and B. Eisenberg, Computing induced charges in inhomogeneous dielectric media: Application in a Monte Carlo simulation of complex ionic systems, *Phys. Rev. E* **69**, 046702 (2004).
- [32] P.-O. Persson and G. Strang, A simple mesh generator in MATLAB, *SIAM Rev.* **46**, 329 (2004).
- [33] T. Poppe, J. Blum, and T. Henning, Analogous experiments on the stickiness of micron-sized preplanetary dust, *Astrophys. J.* **533**, 454 (2000).
- [34] R. G. Harrison, E. Barth, F. Esposito, J. Merrison, F. Montmessin, K. L. Aplin, C. Borlina, J.-J. Berthelier, G. Déprez, W. M. Farrell, I. M. P. Houghton, N. O. Renno, K. A. Nicoll, S. N. Tripathi, and M. Zimmerman, Applications of electrified dust and dust devil electrodynamics to martian atmospheric electricity, *Space Sci. Rev.* **203**, 299 (2016).
- [35] F. Chowdhury, B. Elchamaa, M. Ray, A. Sowinski, A. Passalacqua, and P. Mehrani, Apparatus design for measuring electrostatic charge transfer due to particle-particle collisions, *Powder Technol.* **361**, 860 (2020).
- [36] T. Miura, T. Koyaguchi, and Y. Tanaka, Measurements of electric charge distribution in volcanic plumes at Sakurajima volcano, Japan, *Bull. Volcanol.* **64**, 75 (2002).
- [37] J. S. Gilbert, S. J. Lane, R. S. J. Sparks, and T. Koyaguchi, Charge measurements on particle fallout from a volcanic plume, *Nature (London)* **349**, 598 (1991).
- [38] T.-L. Bo, H. Zhang, and X.-J. Zheng, Charge-to-mass ratio of saltating particles in wind-blown sand, *Sci. Rep.* **4**, 5590 (2014).
- [39] E. Grün, M. Horanyi, and Z. Sternovsky, The lunar dust environment, *Planet. Space Sci.* **59**, 1672 (2011).
- [40] M. Horányi and J. Szalay, Dust charge measurements by the lunar dust experiment, in *2015 IEEE Aerospace Conference (IEEE, 2015)*, pp. 1–5.
- [41] M. M. Abbas, D. Tankosic, P. D. Craven, J. F. Spann, A. LeClair, and E. A. West, Lunar dust charging by photoelectric emissions, *Planet. Space Sci.* **55**, 953 (2007).
- [42] G. R. Olhoeft and D. W. Strangway, Dielectric properties of the first 100 meters of the moon, *Earth Planet. Sci. Lett.* **24**, 394 (1975).
- [43] L. D. Landau, J. S. Bell, M. Kearsley, L. Pitaevskii, E. Lifshitz, and J. Sykes, *Electrodynamics of Continuous Media*, The Course of Theoretical Physics Vol. 8 (Elsevier, 2013).
- [44] R. Allen, J.-P. Hansen, and S. Melchionna, Electrostatic potential inside ionic solutions confined by dielectrics: A variational approach, *Phys. Chem. Chem. Phys.* **3**, 4177 (2001).
- [45] K. Barros, D. Sinkovits, and E. Luijten, Efficient and accurate simulation of dynamic dielectric objects, *J. Chem. Phys.* **140**, 064903 (2014).
- [46] A. Zangwill, *Modern Electrodynamics* (Cambridge University Press, 2013).
- [47] G. Liu, J. S. Marshall, S. Q. Li, and Q. Yao, Discrete-element method for particle capture by a body in an electrostatic field, *Intl. J. Numer. Methods Eng.* **84**, 1589 (2010).
- [48] J. S. Marshall and S. Li, *Adhesive Particle Flow* (Cambridge University Press, 2014).
- [49] G. Grosjean and S. Waitukaitis, Single-collision statistics reveal a global mechanism driven by sample history for contact electrification in granular media, *Phys. Rev. Lett.* **130**, 098202 (2023).
- [50] P. M. Ireland, Dynamic particle-surface tribocharging: The role of shape and contact mode, *J. Electrostat.* **70**, 524 (2012).
- [51] L. Cheng and S. L. Soo, Charging of dust particles by impact, *J. Appl. Phys.* **41**, 585 (1970).
- [52] F. Chowdhury, M. Ray, A. Sowinski, P. Mehrani, and A. Passalacqua, A review on modeling approaches for the electrostatic charging of particles, *Powder Technol.* **389**, 104 (2021).
- [53] H. Grosshans and M. V. Papalexandris, A model for the non-uniform contact charging of particles, *Powder Technol.* **305**, 518 (2017).
- [54] T. Siu, J. Cotton, G. Mattson, and T. Shinbrot, Self-sustaining charging of identical colliding particles, *Phys. Rev. E* **89**, 052208 (2014).
- [55] D. J. Lacks and T. Shinbrot, Long-standing and unresolved issues in triboelectric charging, *Nat. Rev. Chem.* **3**, 465 (2019).
- [56] T. Steinpilz, F. Jungmann, K. Joeris, J. Teiser, and G. Wurm, Measurements of dipole moments and a Q-patch model of collisionally charged grains, *New J. Phys.* **22**, 093025 (2020).
- [57] Y. I. Sobolev, W. Adamkiewicz, M. Siek, and B. A. Grzybowski, Charge mosaics on contact-electrified dielectrics result from polarity-inverting discharges, *Nat. Phys.* **18**, 1347 (2022).
- [58] G. Grosjean, S. Wald, J. C. Sobarzo, and S. Waitukaitis, Quantitatively consistent scale-spanning model for same-material tribocharging, *Phys. Rev. Mater.* **4**, 082602(R) (2020).
- [59] G. Grosjean and S. Waitukaitis, Asymmetries in triboelectric charging: Generalizing mosaic models to different-material samples and sliding contacts, *Phys. Rev. Mater.* **7**, 065601 (2023).
- [60] T. Matsuyama and H. Yamamoto, Charge relaxation process dominates contact charging of a particle in atmospheric conditions, *J. Phys. D* **28**, 2418 (1995).
- [61] T. Matsuyama and H. Yamamoto, Characterizing the electrostatic charging of polymer particles by impact charging experiments, *Adv. Powder Tech.* **6**, 211 (1995).
- [62] G. Lu, J. R. Third, and C. R. Müller, Discrete element models for non-spherical particle systems: From theoretical developments to applications, *Chem. Eng. Sci.* **127**, 425 (2015).